Research Article

Investigation of Fe-Doped Graphitic Carbon Nitride-Silver Tungstate as a Ternary Visible Light Active Photocatalyst

Eid H. Alosaimi,[1] Nadia Azeem,[2] Noor Tahir,[2] Asim Jilani ⓘ,[3] Muhammad Zahid ⓘ,[2] Salman. S. Alharthi,[4] Javed Iqbal ⓘ,[2] Muhammad Yaseen,[5] Zulfiqar Ahmad Rehan ⓘ,[6] and Imran Shahid ⓘ[7]

[1]*Department of Chemistry, College of Science, University of Bisha, P.O. Box 511, Bisha 61922, Saudi Arabia*
[2]*Department of Chemistry, University of Agriculture, Faisalabad 38040, Pakistan*
[3]*Center of Nanotechnology, King Abdulaziz University, Jeddah, Saudi Arabia*
[4]*Department of Chemistry, College of Science, Taif University, P.O. Box 11099, Taif 21944, Saudi Arabia*
[5]*Department of Physics, University of Agriculture Faisalabad, Faisalabad, Pakistan*
[6]*Department of Polymer Engineering, National Textile University Faisalabad, Pakistan*
[7]*Environmental Science Centre, Qatar University, Doha, P.O. Box 2713, Qatar*

Correspondence should be addressed to Muhammad Zahid; rmzahid@uaf.edu.pk and
Zulfiqar Ahmad Rehan; zarehan@ntu.edu.pk

The rapid population growth and economic development have largely contributed to environmental pollution. Various advanced oxidation processes have been used as the most viable solution for the reduction of recalcitrant pollutants and wastewater treatment. Heterogeneous photocatalysis is one of the broadly used technologies for wastewater treatment among all advanced oxidation processes. Graphitic carbon nitride alone or in combination with various other semiconductor metal oxide materials acts as a competent visible light active photocatalyst for the removal of recalcitrant organic pollutants from wastewater. Rational designing of an environment-friendly photocatalyst through a facile synthetic approach encounters various challenges in photocatalytic technologies dealing with semiconductor metal oxides. Doping in $g-C_3N_4$ and subsequent coupling with metal oxides have shown remarkable enhancement in the photodegradation activity of $g-C_3N_4$-based nanocomposites owing to the modulation in $g-C_3N_4$ bandgap structuring and surface area. In the current study, a novel ternary Fe-doped $g-C_3N_4/Ag_2WO_4$ visible light active photocatalyst was fabricated through an ultrasonic-assisted facile hydrothermal method. Characterization analysis included SEM analysis, FTIR, XRD, XPS, and UV-Visible techniques to elucidate the morphology and chemical structuring of the as-prepared heterostructure. The bandgap energies were assessed using the Tauc plot. The ternary nanocomposite (Fe-CN-AW) showed increased photodegradation efficiency (97%) within 120 minutes, at optimal conditions of pH = 8, catalyst dose = 50 mg/100 ml, an initial RhB concentration of 10 ppm, and oxidant dose 5 mM under sunlight irradiation. The enhanced photodegradation of rhodamine B dye by ternary Fe-CN-AW was credited to multielectron transfer pathways due to insertion of a Fe dopant in graphitic carbon nitride and subsequent coupling with silver tungstate. The data were statistically assessed by the response surface methodology.

1. Introduction

Water constitutes a major part of the planet Earth. Almost 98% of this water is seawater and cannot be used for drinking purposes because of the high salt content. Approximately 2% of water is drinkable [1]. Extensive contamination due to global industrialization, commercialization, and agricultural practices has led to the release of organic pollutants that immensely polluted the freshwater reservoirs. Hence, water pollution has emerged as one of the foremost global

environmental challenges. Wastewater discharged from industries and various human activities has caused perilous environmental impacts. An alarming population is suffering every day due to the unavailability of clean drinking water. This gross negligence from various industrial units for releasing wastewater without any treatment into freshwater streams has posed grave threats to human health [2].

Previously, conventional methods such as activated carbon adsorption, filtration, extraction, oxidation, ultrafiltration, electrolysis, chemical oxidation, and biological treatment were used which usually caused incomplete mineralization of pollutants. The shortcomings of these conventional methods were overcome with progressive research in the development of various advanced oxidation technologies. Advanced oxidation processes (AOPs) were firstly utilized in the early 1980s for water treatment and purification. In wastewater treatment, hydroxyl radicals act as strong oxidizing agents, breaking down complex organic pollutants and converting them into less harmful products [3]. Advanced oxidation processes include ozone, Fenton, heterogeneous photocatalysis, sonolysis, catalytic wet air oxidation, and electrochemical oxidation. Sometimes, these processes can combine to produce strong oxidizing radicals that attack any pollutant in the water without distinction and convert them into nonharmful compounds such as carbon dioxide, water, and inorganic ions. AOPs can make use of different semiconductor photocatalysts such as binary or ternary metal oxides and carbon-based support materials [4].

Heterogeneous photocatalysis based on metal-oxide-based semiconductor materials has been employed widely for the degradation of recalcitrant pollutants. Among these conventional semiconductor materials, a new carbon-based photocatalyst graphitic carbon nitride (g-C_3N_4) is being investigated for the fabrication of heterostructures for enhanced degradation under sunlight irradiation. Graphitic carbon nitride is an excellent visible light active and two-dimensional polymeric compound that is highly stable chemically and thermally and has a tunable bandgap from 1.7 eV to 2.8 eV [5]. The medium bandgap range of g-C_3N_4, its chemical and thermal stability, polymeric structure, and simple synthesis methods make it an excellent visible light active photocatalyst and a good semiconductor material for the conversion of solar energy [6]. But, the catalytic performance of g-C_3N_4 alone is hindered because of some limitations such as fast charge carrier recombination [7]. The limitations due to fast e^-/h^+ recombination of g-C_3N_4-based photocatalysts can be addressed using various strategies including doping and coupling with metal oxides [8]. The photoresponse of g-C_3N_4 can be enhanced through doping various transition metals including Fe, Mn, Cu. Co, Ni, and Mo and coupling with other metal oxides to enhance visible light response [9]. g-C_3N_4 support-based photocatalysts are now frequently used in various applications of heterogeneous photocatalysis because these photocatalysts profoundly satisfy environmental requirements of green photocatalysis and the formation of hybrid structures [10]. Doping of a transition metal in g-C_3N_4 lattices alters the physical and chemical properties and enhances the visible

light absorption response for degradation of pollutants by changing the structure and surface area of g-C_3N_4 [11]. Iron (Fe) has proved to be an excellent candidate for doping with graphitic carbon nitride because of its existence in various oxidation states. Insertion of Fe into g-C_3N_4 has shown enhancement in electrochemical conductivity and light absorption ability [12]. Silver tungstate (Ag_2WO_4) is a ternary semiconductor metal oxide having a bandgap between 2.8 eV and 3.1 eV. This ternary metal oxide has been gaining attention because of its better light-harvesting ability and photoluminescence characteristics. Silver tungstate (AW) is functionalized by coupling with other photoactive materials to increase the photoresponse and improve its stability [13].

Hence, it is the necessity of time to synthesise such visible light-reactive ternary systems that are more efficient than those utilized in conventional methods for wastewater remediation. This work was proposed for the investigation of rhodamine B (RhB) dye degradation by ternary Fe-doped g-C_3N_4/Ag_2WO_4 nanocomposite. To the best of our knowledge, this composite has not been studied earlier for the photodegradation of organic pollutants. Iron-doped graphitic carbon nitride was coupled with silver tungstate in which WO_4 has attracted attention due to high chemical and thermal stability and has reasonable electron transfer behavior. g-C_3N_4 and WO_4 have almost similar bandgaps [14]. The degradation of rhodamine B (RhB) dye was analyzed over Fe/g-C_3N_4 (Fe–CN), g-C_3N_4/Ag_2WO_4 (CN-AW), and Fe-doped g-C_3N_4 -Ag_2WO_4/(Fe-CN-AW). The photocatalytic activity of these three catalysts towards RhB degradation was studied under sunlight. The effect of various parameters, for example, pH, oxidant dose, irradiation time, and catalyst dose, was optimized. The interaction of various parameters was studied using the response surface methodology (RSM). The catalysts were characterized by Fourier transform infrared spectroscopy (FTIR), scanning electron microscopy, X-ray diffraction (XRD), XPS, and UV-Vis techniques.

2. Experimental

2.1. Regents and Materials. Melamine ($C_6H_6N_6$ > 99%) and silver nitrate ($AgNO_3$; 99.9% purity) were purchased from DAEJUNG, sodium tungstate dihydrate ($Na_2WO_4.2H_2O$; 97% purity) and ethanol (C_2H_5OH; 95.6% purity) were purchased from UNI-Chem, ferric chloride hexahydrate ($FeCl_3.6H_2O$; > 99% purity) and hydrogen peroxide (H_2O_2; 35% purity) were purchased from Merck, sodium hydroxide (NaOH; 98–100.5% purity) and hydrochloric acid (HCl; 35% purity) were purchased from Sigma-Aldrich, and rhodamine B ($C_{28}H_{31}ClN_2O_3$; 92% purity) was purchased from Pub-Chem. Analytical-grade chemicals and solvents were used in all experiments without additional purification. During the whole experimental study, distilled water was utilized.

2.2. Synthesis of g-C_3N_4. Synthesis of g-C_3N_4 was carried out in a muffle furnace (AB UMEGA SNOL-3/1100) by condensation of melamine. The 5 g mass of melamine was measured and placed in a ceramic crucible, covered

completely, and then, placed in a muffle furnace. Melamine was heated at 20°C per minute for about 2 hours, and the temperature gradually rose until it reached the final temperature. The terminal temperatures were 500°C, 550°C, and 600°C. Then, crucibles containing the sample were chilled to 25°C temperature, and the product formed was ground by using a pestle and mortar [15].

2.3. Synthesis of CN-AW.

To prepare the Ag_2WO_4/g-C_3N_4 composite, sodium tungstate (0.1 mmol/L) and silver nitrate (0.2 mmol) were added to 40 ml deionized H_2O. To the abovementioned mixture, 1 g of previously prepared g-C_3N_4 was added. Then, the whole mixture was sonicated to get a homogenous solution at a temperature of 20°C for about half an hour. This uniform mixture was gradually poured into a 50 ml capacity autoclave having a Teflon-line. After transferring the mixture into the autoclave, it was heated at 180°C for 12 hours in an electric oven. After that, it was filtered and cleaned with distilled H_2O until its pH became neutral. It was dried at 60°C for 5 hours after filtration to obtain the final product, as shown in Figure 1(b) [16].

2.4. Synthesis of Fe-CN.

Iron-doped graphitic carbon nitride (Fe–CN) was synthesised by a simple process in which 0.5 M (FeCl$_3$. 6H$_2$O) was mixed in 50 ml ethanol. Then, 0.5 g of graphitic carbon nitride was dissolved into the abovementioned solution with constant stirring and stirred magnetically for two hours at room temperature. The suspension obtained after stirring was then centrifuged at 6000 revolutions per minute for fifteen minutes, and distilled water, as well as acetone, was used to wash it several times until it became neutral. Then, it was dried at room temperature, as shown in Figure 1(c) [17].2.5. Hydrothermal Synthesis of Ternary Fe-CN-AW.

A hydrothermal method was used for the synthesis of the ternary iron-doped graphitic carbon nitride/silver tungstate (Fe-CN-AW) nanocomposite. In the first step, 2.5 mmol (0.28 g) of sodium tungstate (Na$_2$WO$_4$.2H$_2$O) was dissolved completely in 40 ml distilled water with magnetic stirring. Another solution was made in which 5 mmol (0.29 g) of AgNO$_3$ was added to 20 ml of distilled H$_2$O. Both solutions were mixed slowly under continuous stirring. The previously prepared Fe-doped graphitic carbon nitride (2 mol %) was ultrasonically dispersed in 30 ml of distilled water and added to solution A dropwise. After that, the whole suspension was stirred magnetically for four hours at 25°C temperature till a uniform solution was obtained. The resultant mixture was transferred into an autoclave reactor lined with Teflon at an elevated temperature of 180°C for about 24 hours. The final product was rinsed three times with ethanol and distilled water. Employing an electric oven, the sample was later dried for about 12 hours at 60°C. Figure 1(d) explains the stepwise synthesis of ternary Fe-CNAW heterojunction.

2.5. Characterization and Equipment.

The phase identification, crystalline nature, and crystal structure of Fe–CN, CN-AW, and ternary Fe-doped CN-AW were analyzed by powder XRD (XRD-PANalytical-Xpert pro DY 3805) containing a Ni-β filter and Cu-Kα radiations (1.54059 Å), over a range from 10° to 80° of 2θ values. The identification of various functional groups was recorded using an FTIR spectrophotometer (Agilent Technologies) in the transmission mode, between 650 cm^{-1} and 4000 cm^{-1}. A scanning electron microscope (SEM-JEOL/EO Japan JSM-5910) was used for observing the morphology of all samples. The surface chemical states were analyzed using XPS (XPS system Escalab 250, Thermo Scientific Uk). The optical and photocatalytic properties of doped and undoped nanocomposites were analyzed utilizing a double-beam UV-Vis (Cecil CE 7200) spectrophotometer.

2.6. Photocatalytic Degradation Evaluation.

The photocatalytic degradation of rhodamine B dye was estimated under UV and sunlight irradiation. Different feasibility experiments were initially performed to check the activity of the ternary photocatalyst. For attaining a stage of adsorption-desorption equilibrium between the catalyst surface and pollutant molecule, the RhB solution was placed for about half an hour in the dark with continuous stirring on an orbital shaker. The adsorption was measured by taking 5 ml solution and taking absorbance. The adsorption rate usually starts decreasing after 30 minutes. The whole setup was then brought under sunlight irradiation, and the photodegradation process was started. Similar experiments were performed under ultraviolet radiation as well. Optimization of various parameters for RhB degradation was performed, including pH (2–9), initial RhB concentration (10–50 ppm), oxidant dose (2–15 mM), catalyst dose (10–100 mg), and time of irradiation (20–120 minutes). A UV-Vis spectrophotometer was used to check absorbance at 554 nm by taking a 10 ml clear RhB solution obtained after separation of the composite through centrifugation. The degradation process was also studied in the absence of light by placing a beaker of dye solution in the dark. The blank experiment performed without a catalyst and light revealed no distinct photocatalytic activity, signifying that the reaction was driven by the photocatalytic process over the photocatalytic process of light. The following formula was used to calculate % degradation:

$$\% \text{ degradation} = 1 - \frac{A}{Ao} \times 100, \tag{1}$$

where Ao is described as the initial absorbance and A is the calculated final absorbance after a performed reaction in sunlight. A light meter (HS1010 A) and solar power meter (SM206) were used for measuring the brightness and intensity of sunlight. The measured average light intensity was 1200 W/m^2, and the brightness was measured between the range of 88,000 ± 2000 Lux. The degradation reaction was carried out in the afternoon when the sky was bright and clear. The intensity of the UV light was 254 nm, and the experiment was performed in a UV chamber ZM144 (ZAM ZAM Microtechnologies). The catalyst's reusability was examined by recycling ternary composites by washing with distilled water, drying, and then, reusing till five cycles under sunlight, each at their optimum conditions with 10 ppm RhB solution prepared fresh each time.
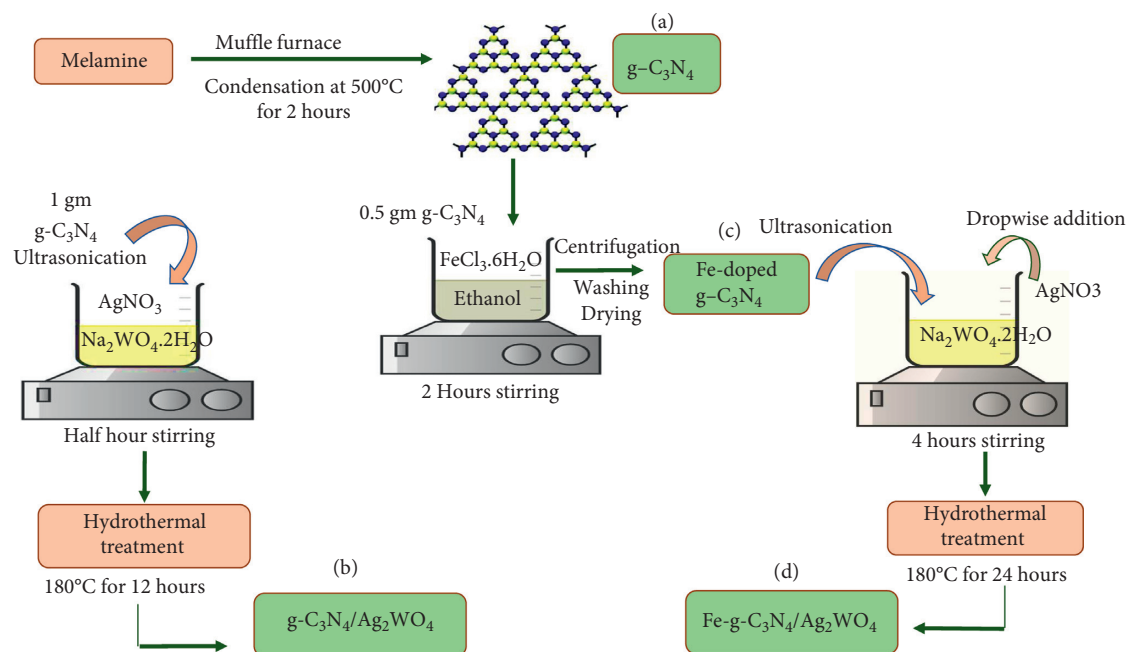
FIGURE 1: Schematic illustration of (a) $g-C_3N_4$, (b) $g-C_3N_4-Ag_2WO_4$, (c) Fe-g-C_3N_4, and (d) Fe-g-C_3N_4/Ag_2WO_4 heterojunctions.

3. Results and Discussion

3.1. FTIR Analysis. The FTIR analysis was recorded between the range of 500 cm^{-1} and 4500 cm^{-1} for the determination of various functional groups present on the surface of the ternary composite. Graphitic carbon nitride was synthesised under varying temperature conditions. FTIR spectra showed all the characteristic transmittance peaks of $g-C_3N_4$ confirming the synthesis of graphitic carbon nitride, without any prominent change at different temperatures, as shown in Figure 2(f). The broad absorption band of pristine $g-C_3N_4$ can be seen in all the samples synthesised at various temperatures. The bands beyond 3000 cm^{-1} up to 3300 cm^{-1} are due to N–H bond stretching vibration resulting from partial condensation of amino acids. The series of peaks appearing between 1200 cm^{-1} and 1620 cm^{-1} shows the stretching vibrations of CN heterocycles. At 500°C, two bands were seen at 1598 cm^{-1} and 1395 cm^{-1}. The peaks at 1228 cm^{-1} and 1395 cm^{-1} matched well with $g-C_3N_4$. At 550°C in the spectrum, N-H stretching vibration was observed by a peak at 3151 cm^{-1} while the vibration bands from 1200 cm^{-1} and 1800 cm^{-1} are related to $g-C_3N_4$. The spectrum corresponds to 550°C and at 15°C/min has bands in the range from 1300 cm^{-1} to 1828 cm^{-1}, representing vibrations of C-N bonds. The FTIR spectrum of Fe-CN, CN-AW, and Fe-CN-AW was compared and shown in Figures 2(c)–2(e), respectively. In the Fe-CN spectrum, a broad peak appeared at 3078 cm^{-1} which is a distinctive peak of the N-H group. It is due to the vibrational mode of the residual N-H group of graphitic carbon nitride. The vibrational mode of the C-N band was shown by a range of peaks from 1200 cm^{-1} to 1600 cm^{-1}. The peaks appearing at 1234 cm^{-1}, 1385 cm^{-1}, and 1578 cm^{-1} related to the CN heterocycles corresponding to C-NH-C, C-N, and C=N confirm fabrication of graphitic carbon nitride in all samples [18]. A small additional peak at 2145 cm^{-1} indicates the Fe^{3+} dopant's existence in a polymeric network of $g-C_3N_4$ [19]. A peak near 807 cm^{-1} shows the occurrence of a triazine ring of aromatic nature. The prominent and distinctive $g-C_3N_4$ bands seem to shift towards lower wavenumbers, and the intensity of FTIR spectra peaks is decreased in the Fe-CN-AW composite. This shift indicates the weakening of C–N and C=N as a result of interaction between $g-C_3N_4$ and Fe [17]. In the CN-AW composite spectrum, a broad peak was presented at 3153 cm^{-1} which is owing to the N-H band stretching mode [20]. The peak at 2381 cm^{-1} is owed to amide linkages, and carbonyl group presence is represented by a peak at 1600 cm^{-1} [21]. There is a range of peaks from 1200 cm^{-1} to 1600 cm^{-1} similar to the Fe-CN spectrum which is due to the IR active vibrational mode of the C-N bond. Two peaks at 739 cm^{-1} and 630 cm^{-1} show O-W-O and W-O-W groups that are a special feature of tetrahedral tungstates. All the peaks present in pure $g-C_3N_4$ remain intact in ternary the Fe-g-C_3N_4/Ag_2WO_4 composite.

3.2. XRD Analysis. To determine the various phases and crystal structure of CN, Fe-CN, CN-AW, and Fe-CN-AW, XRD characterization was performed from 2θ values 10° to 80°. The XRD spectra reveal peaks at 27.7° which are in agreement with the actual XRD peaks of $g-C_3N_4$ (JCPDS-87-1526) [22]. The diffraction peak at 27.7° indexed to the (002) plane is a characteristic of $g-C_3N_4$, showing stacking of aromatic systems between $g-C_3N_4$ layers [23]. The XRD pattern of Fe–CN exhibited no significant difference from CN except for a slight shift and gradual decrease in the peak
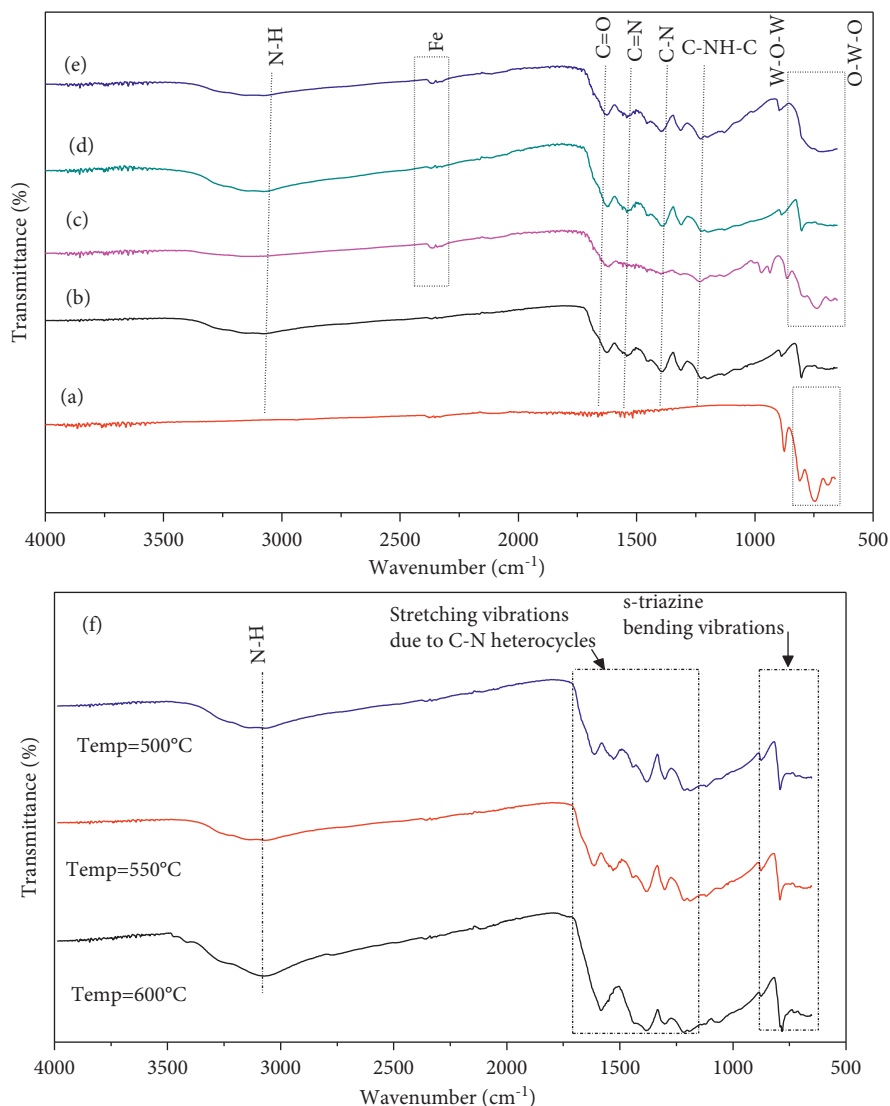
FIGURE 2: FTIR spectra of (a) AW, (b) g-C$_3$N$_4$, (c) Fe–CN, (d) CN-AW, (e) Fe-CN-AW, and (f) g-C$_3$N$_4$ at various annealing temperatures.

intensity of the (002) facet in Fe-CN, AW-CN, and Fe-CN-AW. The incorporation of an iron dopant in CN did not change the g-C$_3$N$_4$ crystal structure, as no peak of Fe was identified in the samples [19]. The diffraction peaks of g-C$_3$N$_4$ remain intact which shows that the doping of iron does not change the peaks of g-C$_3$N$_4$ but the intensity of the peaks in the final composite is reduced, confirming effective insertion of the dopant [24]. The XRD data displayed well-defined diffraction peaks consistent with planes (301), (002), (231), (400), (402), (233), (460), and (462), observed at 2θ values 28.4°, 30.58°, 31.67°, 32.88°, 45.4°, 54.9°, 56.9, and 58.04°, respectively, as shown in Figure 3, and are coherent with the corresponding planes of Ag$_2$WO$_4$ (JCPDS# 34–0061) [13]. All the characteristic peaks of g-C$_3$N$_4$ and Ag$_2$WO$_4$ are present in the Fe-doped ternary composite but with lesser intensities than the undoped CN-AW and Fe-CN composites. However, the strong intensity of diffraction peaks in both the composites suggests the successful

synthesis and crystalline nature of composites [25]. There is also a very slight shift of the peak at a diffraction angle of $2\theta = 45.3°$, corresponding to a plane (402) towards higher diffraction angles, indicating the insertion of Fe into the host composite lattice. X-ray diffraction is an effective analysis technique to determine the size of nanocrystallites in bulk nanocrystalline materials. The average crystallite size of Fe-doped CN-AW, undoped CN-AW, and Fe-CN catalysts was assessed using the Debye–Scherrer formula.

$$D = \frac{K\lambda}{\beta \cos \theta}, \qquad (2)$$

where K is the Scherrer constant (0.94), β explains the full width at half maximum (FWHM) of each diffraction peak, θ is the angle of diffraction, λ is the radiation wavelength, and D is the average crystallite size in nm. The average crystallite size of Fe-CN, CN-AW, and Fe-CN-AW was calculated to be
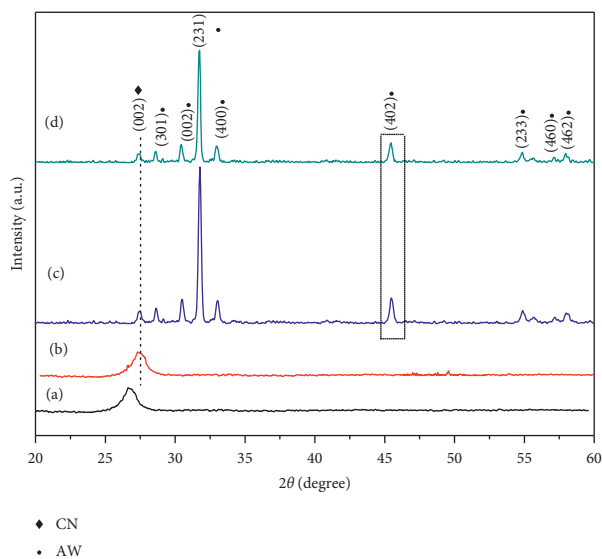
Figure 3: XRD spectra of (a) CN, (b) Fe-CN, (c) CN-AW, and (d) Fe-CN-AW.

19.78 nm, 14.29 nm, and 13.34 nm, respectively. The decreased crystallite size indicates the presence of oxygen vacancies as a result of Fe doping which hinders the further growth of nanoparticles [26]. The defects caused by Fe doping reduce recombination chances of charge carriers and enhance photocatalytic activity [27].

3.3. Scanning Electron Microscopy (SEM) Analysis. The SEM analysis was used to study the morphology of Fe-g-C_3N_4, AW-CN, and Fe-CN-AW nanocomposites at different resolutions. Figures (4(a) and 4(b)) show the morphology of Fe-CN, revealing uniform and smooth sheets of g-C_3N_4 and aggregation of particles as an outcome of Fe doping on g-C_3N_4 sheets. In Figures (4(c) and 4(d)), it can be seen that Ag_2WO_4 is dispersed irregularly in the form of small spherical particles on the surface of g-C_3N_4 sheets. The coupling of AW and g-C_3N_4 reveals that the coupling has not affected the morphology of AW spheres. Instead, the g-C_3N_4 aggregates got attached to the surface of silver tungstate. These particles have smooth particle size distribution when present in the form of nonagglomerated particles. The g-C_3N_4 serves as a support on which Ag_2WO_4 particles are embedded. Figures 4(e) and 4(f) signify the coupling between Fe-CN and AW in the ternary composite. These SEM images illustrate those agglomerates of Fe-CN were successfully anchored over AW. In the presence of Fe, the agglomeration and stacking of particles were enhanced as compared to simple AW-CN. Similar results of doping and coupling were also reported in previous studies [28].

3.4. XPS Analysis. The surface chemical composition and chemical binding states of all the photocatalytic samples were analyzed using XPS analysis. The elemental composition of the Fe-CN-AW nanocomposite examined through an XPS survey scan reveals the presence of peaks at Ag3d (368.3 eV), W (37.51 eV), O1s (530.2 eV), C1s (284.07 eV),

Fe (710.8 eV), and N1s (396.21 eV), as shown in Figure 5(a). The C1s peak position indexed at 285.2 eV in all three samples indicates the presence of adventitious residual carbon and is ascribed to the tertiary carbon N=C-N_2 in the Fe-g-C_3N_4 lattice. The N1s peak present at 396.21 eV is credited to the triazine rings of g-C_3N_4 and the uncondensed terminal amino groups [20]. The W4$f_{7/2}$ and W 4$f_{5/2}$ peaks at 35.44 eV and 37.5 eV, respectively, in the W4f spectrum of Ag_2WO_4 are ascribed to WO_4^{2-}. The Ag 3d spectra show two characteristic peaks at 372.1 eV and 368.3 eV which are typically allotted to Ag 3$d_{3/2}$ and Ag3$d_{5/2}$, respectively. The peaks of Ag3d and W4f XPS spectra moved towards the higher binding energies in the Fe-CN-AW. The Fe 2p$_{3/2}$ at a binding energy of 710.8 eV is ascribed to Fe^{3+} ions. The binding energy of 710.8 eV lies inside the binding energy range of the Fe^{3+} valence state (710–711.8 eV). The Fe 2p$_{1/2}$ showed a characteristic peak of Fe^{3+} at 731.54 eV [19]. The atomic percentage of O1s, N1s, C1s, Ag3p3, Ag3d, W4f, and Fe2p3 in Fe-CN-AW is 30.3%, 22.2%, 13.3%, 13.2%, 10.1%, 7.1%, and 4.3%, respectively, while the atomic percentage of O1s, N1s, C1s, Ag3p3, Ag3d, and W4f in undoped counterpart is 18.9%, 19.4%, 24.3%, 4.6%, 16.0%, 12.8%, and 8.6 atomic percentages, respectively, as shown in Figure 5(b).

In XPS spectra, the O1s peak found at a binding energy of 528.18 eV is ascribed to the chemisorbed water molecules on the surface of the sample. Furthermore, oxygen functional groups were investigated through O1s spectra, as shown in Figure 5(c). The peaks were found around 530.2 ± .05 eV, 531.6 ± .06, and 533.5 ± .04 eV and attributed to the metallic contribution of oxygen (O $_{Metallic}$), carbonyl (C=O), and carboxyl (OH), respectively [29, 30]. However, their contributions varied with the addition of dopants. Therefore, Fe-CN showed a total contribution of O $_{Metallic}$ around 74.85%, while C=O and OH were around 20.93 and 4.23 atomic percentage. The C=O was noticed at around 41.32% and 27.49% for CN-AW and Fe-CN-AW, respectively. Moreover, the contribution of OH was maximum for Fe-CN-AW and was around 22.59%. This increment of OH is also favorable to enhance the photocatalytic activity of g-C_3N_4-based materials [31].

3.5. Optical Analysis. To further understand the optical properties of the prepared nanocomposites, an evaluation of optical response was carried out by taking UV-Vis spectra and then determining the bandgap energies of nanocomposites Fe-CN, CN-AW, and Fe-CN-AW in the range of 200–800 nm. Using the Tauc plot, the absorption edge of the ternary Fe-CN-AW nanocomposite was found in the visible range (2.56 eV), as shown in Figure 6. The Fe-CN-AW exhibited a better light absorption range as related to other composites. Fe doping has shown enhancement in photodegradation upon improved prospect of charge carrier production upon light irradiation, eventually increasing photodegradation. The following formula was used to assess the catalyst's bandgap energies [13]:

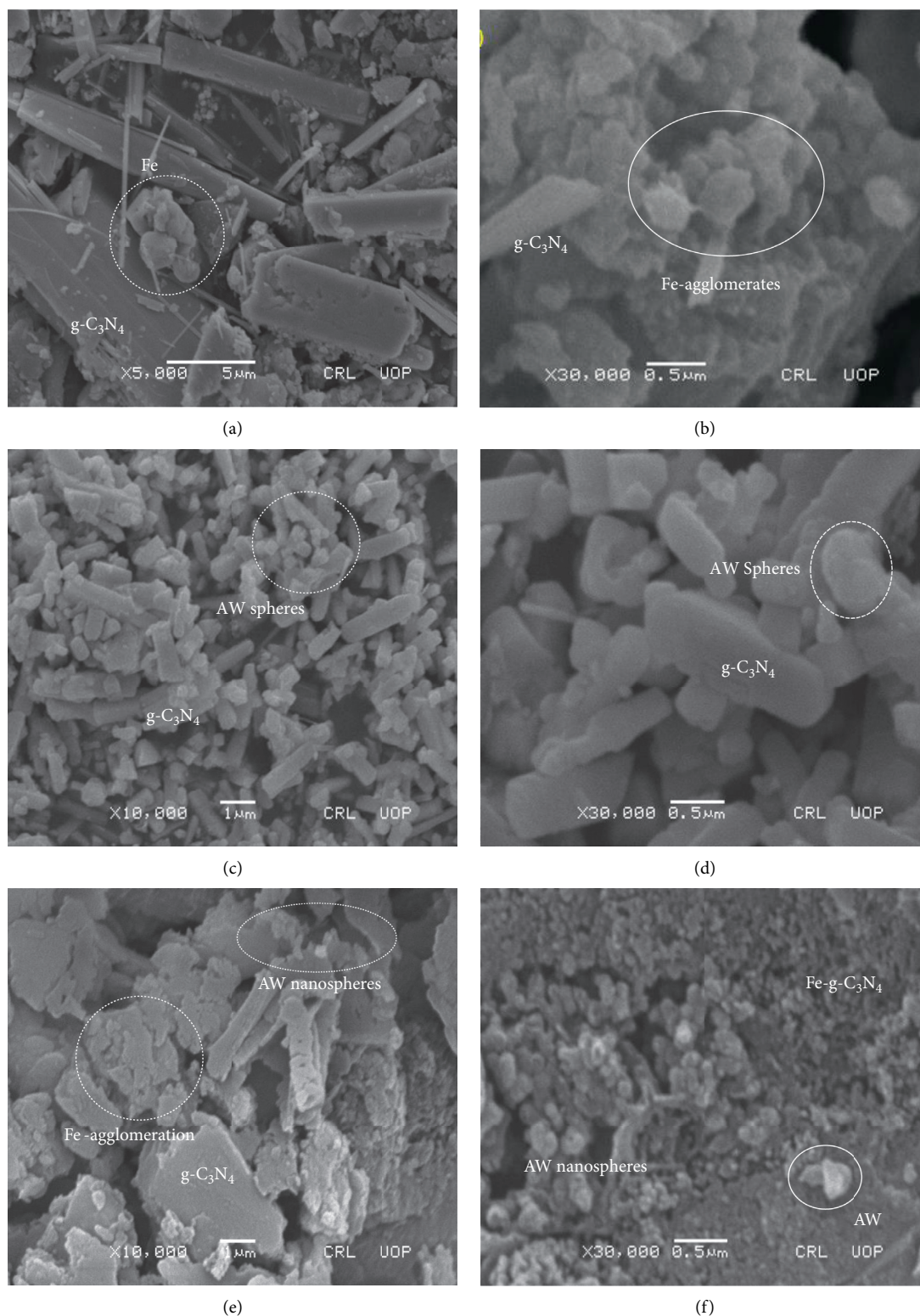$$(\alpha h v)^2 = B (h v - E g). \tag{3}$$

(a)

(b)

(c)

(d)

(e)

(f)

FIGURE 4: SEM analysis of (a and b) Fe-CN, (c and d) CN-AW, and (e and f) Fe-CN-AW.

In this equation, energy $(E) = h\nu$, at $(\alpha h\nu = 0)$, where $(\alpha h\nu)^2$ is plotted versus energy (eV). At $h\nu$ value, energy is calculated and then extrapolated to $\alpha = 0$. The light frequency, absorption coefficient, and proportionality constant are explained by $(\alpha, B,$ and $\nu)$, respectively. The studies reveal that iron doping has strengthened the light absorption response of the ternary photocatalyst in the visible region. The estimated band gap energies were 2.56 eV, 2.8 eV, and 3.3 eV for Fe-CN/AW, Fe-CN, and CN-AW, respectively. The presence of g-C_3N_4 as support
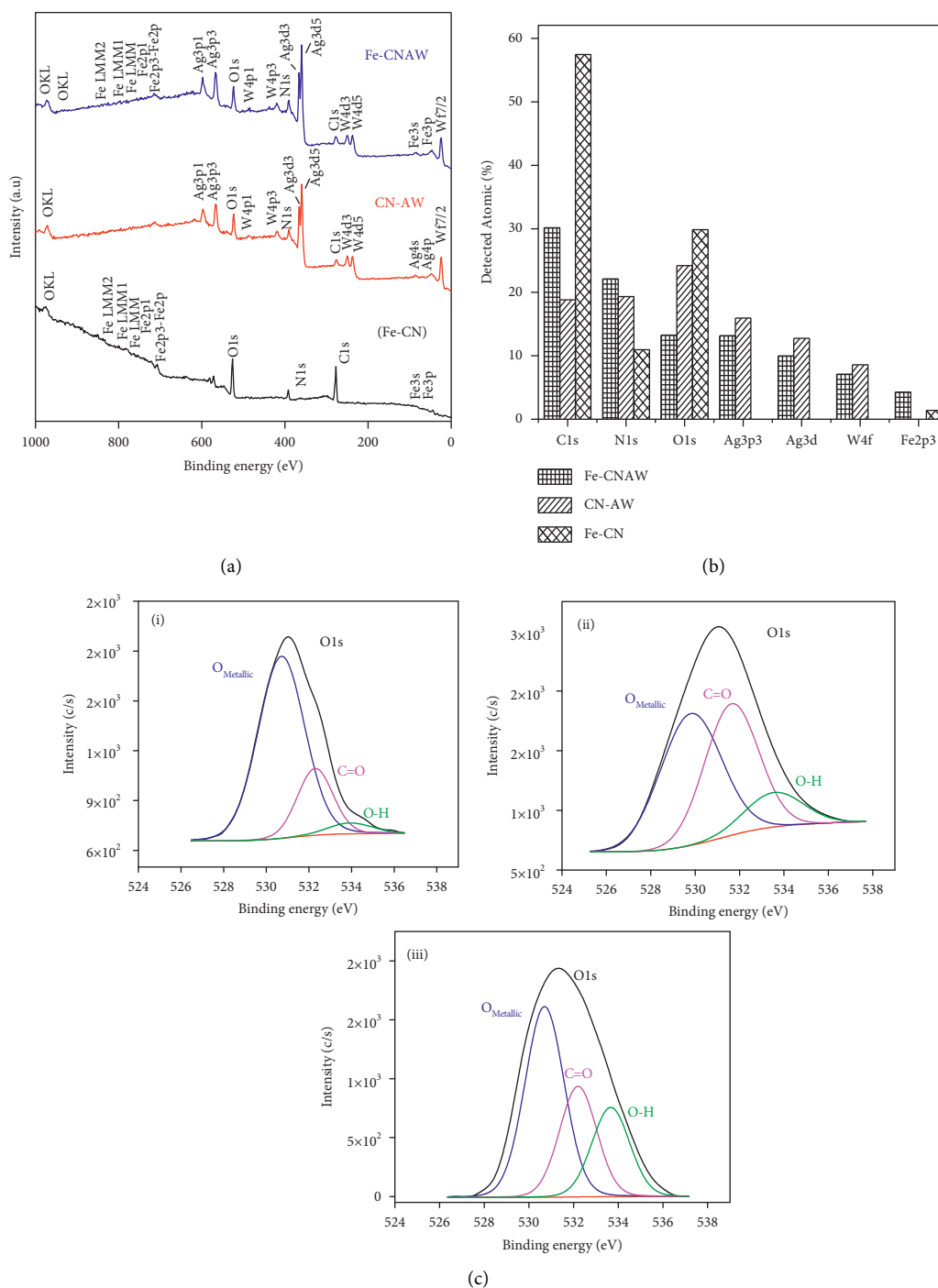
(a)

(b)

(c)

FIGURE 5: XPS (a) survey spectrum and (b) atomic percentage of various elements in Fe–CN, CN-AW, and Fe-CN-AW; (c) O1s functional groups for (i) Fe–CN, (ii) CN-AW, and (iii) Fe-CN-AW.

narrowed the bandgap of the ternary composite, suggesting efficient separation of charge carriers [23].

4. Operating Parameters Affecting the Photocatalytic Process

The photodegradation process of recalcitrant dyes from the adsorption of molecules of the dye on the photocatalyst's surface to their degradation by reactive radical species is affected by numerous operative parameters. These include pH of the aqueous solution, initial concentration of dyes (IDC), catalyst dose, and intensity of irradiating light sources. These parameters will be discussed in detail as they directly affect the photodegradation of dyes in wastewaters.

4.1. Effect of pH. The photoefficiency of any photocatalytic system is determined by the crucial factor of the pH of
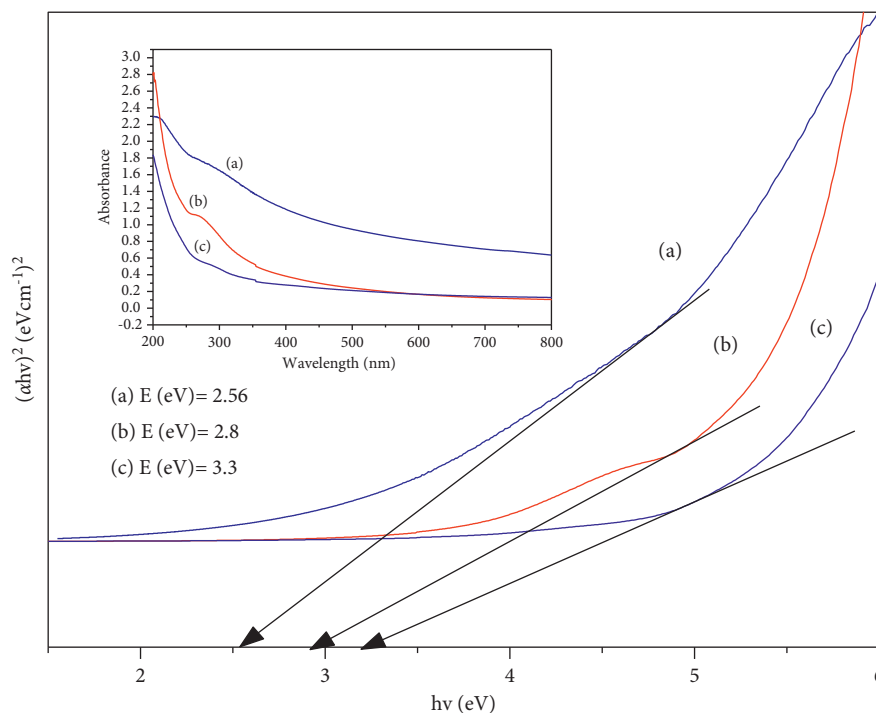
FIGURE 6: Bandgap energy estimation of (a) Fe-CN/AW, (b) Fe-CN, and (c) CN-AW by the Tauc plot method.

aqueous solutions. The pH of a solution affects not only the photocatalytic degradation process but also the rate at which the dye decolorizes the positive hole (h^+) species formed at lower pH values which act as the key oxidation species, while hydroxyl radicals are the key species at higher or neutral pH values for the degradation process. The surface charge characteristics are determined according to their respective point of zero charges (pH_{PZC}). Acid-base characteristics of photocatalysts significantly impact their degradation efficiencies. At $pH < pH_{PZC}$, the surface of the catalyst is positively charged, and hence, it develops an electrostatic attraction for anions and repulsion for cations. Contrary to this, at $pH > pH_{PZC}$, the surface becomes negatively charged and develops an attraction for cations and repulsion for anions [32]. The pH effect on RhB photodegradation was observed by varying pH values. The remaining factors were kept constant in which the catalyst dose was 50 mg/100 mL for doped and 70 mg/100 ml for Fe-CN and CN-AW. IDC was kept at 10 ppm for all composites, and time of irradiation was two hours. Being a cationic dye, upon dissociation in water, RhB is positively charged. The pHPZC of Fe-CN-AW was determined at a pH value of 6.2. The catalyst surface is positively charged at pH values lesser than pHPZC and, hence, repels positively charged RhB molecules. Active sites on the surface of the composite become weaker in an acidic medium, producing fewer hydroxyl radicals, leading to a decline in overall degradation, while active sites existing on the surface exhibited improved production of hydroxyl radicals in the basic medium. Henceforth, at pH values higher than 6.2, the nanocomposite surface becomes negatively charged, attracting positively charged RhB molecules

electrostatically, increasing the adhesion property of pollutant molecules on the composite surface [33]. Therefore, in visible light irradiation, nearly 97% degradation by ternary Fe-CN-AW in two hours was observed in a basic medium at an optimum pH of 8, as shown in Figure 7(a). CN-AW and Fe-CN at pH 7 showed nearly 95% and 90% degradation, respectively.

4.2. Effect of Catalyst Concentration. The effectiveness of the photocatalyst for the degradation process is determined by its concentration in the dye solution. To comprehend the relation between catalyst dose and RhB photodegradation, removal of the 10 ppm RhB solution was studied between the range 10 and 100 mg/100 ml, while all other parameters such as pH = 8 for Fe-CN-AW and pH = 7 for CN-AW and Fe-CN, catalyst dosage 50 mg/100 ml for doped ternary and 70 mg/100 ml for CN-AW and Fe-CN, and irradiation time 120 minutes remained as such. As the photocatalyst dose was augmented from 10 mg to 50 mg, an intensification in RhB degradation was observed, as shown in Figure 7(b). Fe-CN-AW showed optimum degradation at 50 mg/100 ml, whereas CN-AW and Fe-CN showed maximum degradation at 70 mg/100 ml. This increased degradation is credited to increased active sites on the surface of the catalyst, which then leads to more production of hydroxyl radicals, which increases the process of degradation. However, above the optimum catalyst loading limit for each catalyst, the percentage degradation starts decreasing. This is because of the interference of light by the suspension. The additional amount of catalyst causes aggregation of catalyst particles
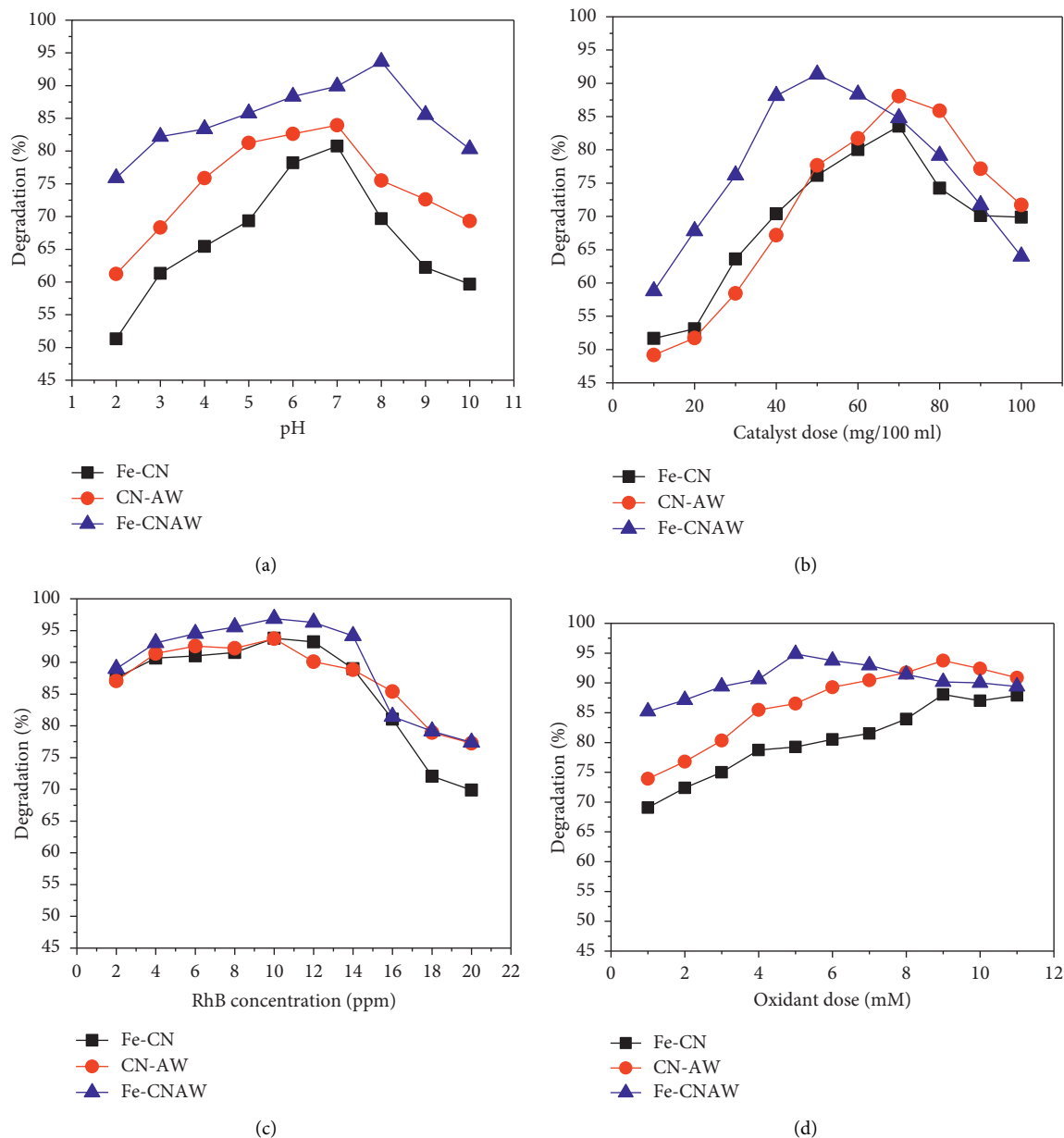
(a)

(b)

(c)

(d)

Figure 7: Optimization of reaction parameters using Fe-CN, CN-AW, and Fe-CN-AW: (a) pH, (b) photocatalyst dose, (c) RhB Initial concentration, and (d) oxidant dose.

and inhibits the light irradiation and subsequent absorption of photons by the catalyst surface, reducing the hydroxyl production and ultimately reducing degradation [34].

4.3. Effect of Initial Dye Concentration.

In the degradation process, the total amount of dye adsorbed on the surface of the photocatalyst plays a key role, not the dye molecules present in the bulk solution. The initial dye concentration is a critical factor for determining the complete adsorption capacity of dye molecules. The degradation efficiency starts decreasing as the concentration of dye is increased, while the amount of photocatalyst used is kept constant. The degradation started decreasing after the concentration of dye was increased, as shown in Figure 7(c). All samples showed maximum degradation at a concentration of 10 ppm, at their optimal values of pH and catalyst dose. The catalyst Fe-CN-AW showed a degradation of 80% up to 14 ppm, after which it started declining. Owing to an increase in the number of dye molecules, more molecules get attached to the photocatalyst surface, resulting in lesser photons reaching the nanocomposite surface [35]. This eventually results in a decline in hydroxyl ion generation and, subsequently, the decolorization process. Previously, reports have revealed

that the dye degradation rate declined as the dye concentration increased. This is because of the reduction in the path length of photons entering the dye solution as the number of dye molecules increases [33].

4.4. Effect of Oxidant Dose.

In the process of photodegradation, oxidants (H_2O_2) have an important role because they hinder the recombination of (e^-–h^+) pairs by capturing the electron. Furthermore, OH radicals are generated from the oxidant by the Ag^{+2} and Fe^{2+} ion interaction. Rhodamine B dye is oxidized completely in the presence of an oxidant (H_2O_2) and a catalyst. In sunlight, the degradation of RhB dye was enhanced by its adsorption on the catalyst surface due to high tendencies of formation of oxidizing species. By the coupling of semiconductors with g-C_3N_4 photocatalysts, degradation is also enhanced. The adsorption ability of g-C_3N_4 is enhanced in the presence of an oxidant. At pH = 7, catalyst dose = 70 mg/100 ml, and oxidant dose = 9 mM, the degradation percentage was 88% for Fe/g-C_3N_4, as represented in Figure 7(d). In the case of the Ag_2WO_4/g-C_3N_4 composite at pH = 7, catalyst concentration = 70 mg, and oxidant dose = 9 Mm, maximum degradation occurs which is 93%, while in the case of Fe-CN-AW at pH = 8, catalyst concentration = 50 mg/100 ml, and oxidant dose = 5 mM, the degradation was equal to 97%.

4.5. Effect of Time.

Light energy is a primary source for starting any photocatalytic process because it provides the maximum energy. It is, therefore, necessary to ascertain light irradiation conditions for a substantial impact on the photodegradation process. The trend of RhB degradation in solar light with time over Fe-CN-AW, CN-AW, and Fe-CN is shown in Figure 8(a), which shows increased degradation with increasing time. The dye solutions having all these catalysts in their optimal doses and other fixed reaction conditions for each catalyst were exposed to sunlight for around 2 hours. The percentage degradation of the treated dye solution was observed by taking a plot of percent degradation versus time. The solution color disappeared exactly after 40 minutes of exposure to light, and degradation was complete after around 120 minutes of light irradiation using the new ternary Fe-CN-AW, but intensity decline was slow with CN-AW and Fe-CN. The disappearance of solution color signifies that color-imparting chromophores are disintegrating slowly with time. Furthermore, kinetic models were fitted to these data in which first-order kinetic was fitted well.

4.6. Kinetics of Photodegradation Reaction.

The first-order kinetic model was applied for RhB photodegradation by the ternary nanocomposite as explained in equation (3).

First-order kinetics:

$$\text{In} \frac{Co}{Ct} = k_1 t. \tag{4}$$

Figure 8(b) displays the linear association among ln (Co/Ct) versus time of reaction; here, Co and C explain the initial and final concentrations. This shows that RhB degradation by the ternary Fe-CN-AW, CN-AW, and Fe–CN follows first-order kinetics. The plot of ln (Co/C) with time is linear. The linear regression slope is equal to the first-order rate constant (k). The higher k values of Fe-CN-AW than binary CN-AW and Fe–CN directs that decolorization by Fe-CN-AW under sunlight is more than that by CN-AW. The R^2 values for first-order reaction for Fe-CN-AW, CN-AW, and Fe-CN-AW suggest that ternary hybrids follow first-order reaction efficiently and doping has accelerated degradation in the presence of sunlight. This explains that Fe-CN-AW exhibits more photoefficiency than other composites. An assessment of correlation coefficients for first-order kinetics is shown in Table 1.

5. Statistical Analysis

The photocatalytic degradation procedure was mostly determined by the widely employed technique RSM which studies the optimization of parameters. In RSM, mathematics is combined with statistics for empirical representation. The purpose of RSM is to optimize photocatalyst response for different parameters to degrade RhB degradation. It works efficiently for experimental studies. It also reduced the noise and expenses of analytical procedures. It minimizes the expenditure of expensive analysis techniques. In the present work, the Fe-CN-AW ternary composite was synthesised by a hydrothermal technique and utilized for RhB degradation. For example, various parameters such as catalyst dose, pH, oxidant dose, and time were optimized by RSM, and absorbance was noted by using a UV-Vis spectrophotometer.

In RSM, for statistical analysis of dye degradation, a central composite design (CCD) was used. According to the CCD, 30 experiments were conducted for the study of the photo-Fenton procedure. Each experimental trial has specific coRhBinations of four elements, e.g., pH, oxidant dose, catalyst dose, and irradiation time. After each experimental trial, percent degradation was calculated and put into a table. Some experimental trials have the same coordination of factors to have the idea of experimental error. Analysis of variance (ANOVA) was used to evaluate the effectiveness of the regression model, as shown in Table 2.

The photodegradation of RhB was optimized using the central composite design (CCD) of the response surface methodology. Among all RSM designs, the CCD method shows high predictability of responses and is the most efficient method for optimizing several variables. The CCD is used for determining the relationship among independent variables and their responses [36].

Based on the results from batch studies, four effective parameters for the degradation of RhB by Fe-CN-AW and their possible interactions were identified using RSM. The pH (2–9), photocatalyst dose (10–80 mg), oxidant dose (2–12 mM), and time (20–180) in minutes were designated as independent variables, and the effect of their interactions was determined using the CCD. The statistical software Design Expert 7 was used for the optimization of parameters. A total of 30 experiments were obtained randomly for
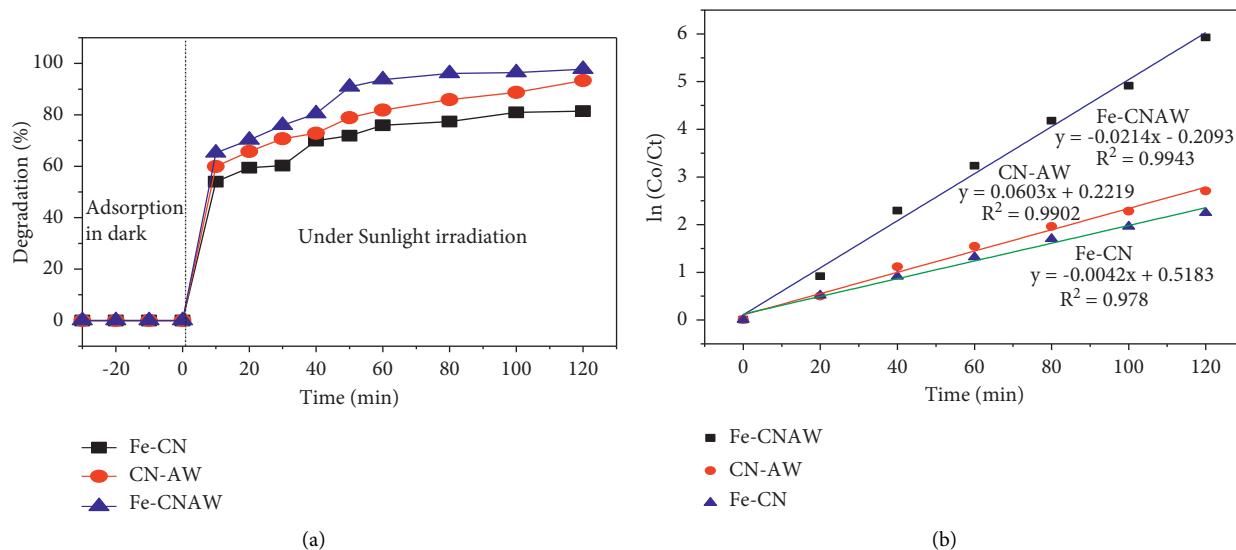
FIGURE 8: (a) RhB degradation by all catalysts as a function of time under sunlight and (b) first-order kinetic model fitting.

TABLE 1: Correlation coefficients (R^2) and kinetic parameters for RhB (Co = 10 ppm) degradation.

Nanocomposites	Optimized reaction conditions			First-order kinetics	
	pH	Catalyst load (mg/ml)	IDC (ppm)	$k1$ (min^1)	R^2
Fe-CN-AW	8	50	10	0.0214	0.9943
CN-AW	7	70	10	0.0603	0.9902
Fe–CN	7	70	10	0.004	0.978

studying the optimized parameters and for maximizing RhB photodegradation. The ANOVA (analysis of variance) was used to analyze the effect of all independent variables on the degradation of dye. The response variable (% degradation) was fitted with the quadratic model for corelating with the experimental variables. The predicted and experimental values are tabulated in Table 2. To understand the association of three variables, a second-order polynomial equation was employed. The quadratic regression model for the degradation of MB is represented by equation (3).

$$
\begin{aligned}
y = {} & \beta_0 + \beta_1 X_1 + \beta_2 X_2 + \beta_3 X_3 + \beta_4 X_4 + \beta_{12} X_1 X_2 + \beta_{13} X_1 \beta X_3 \\
& + \beta_{14} X_1 \beta X_4 + \beta_{11} X_1^2 + \beta_{22} X_2^2 + \beta_{33} X_3^2 + \beta_{44} X_4^2, \\
Y = {} & +88.67 + 7.3 * A + 7.1 * B - 2.83 * C + 6.9 * D + 0.38 * A * B + 1.50 * A * C \\
& + 1.38 * A * D + 0.000 * B * C - 3.12 * B * D + 0.50 * C * D \\
& - 6.65 * A^2 - 1.65 * B^2 - 3.77 C^2 - 2.27 * D^2.
\end{aligned}
\tag{5}
$$

The 3D response was studied for the interactive relationship between the four parameters on dye degradation. For the determination of maximum degradation, 3D surfaces were plotted and taken into consideration. From this, interaction among two independent variables was established, keeping the other variables constant. For the degradation of dye, pH is an efficient parameter. The maximum degradation of RhB dye over Fe-CN-AW was observed at pH = 8 and catalyst dosage = 50 mg in 100 ml of dye solution. Figure 9(a) reveals an enhancement in degradation efficiency by increasing the Fe-CN-AW dose up to an optimal value at pH value = 8. These interactions show the effect of pH on the surface charge properties of the Fe-CN-AW ternary composite, consequently affecting the adsorption of RhB molecules on the surface of the catalyst. Meanwhile, the reaction amongst holes (h$^+$), present on the surface of Fe-CN-AW, and hydroxide ions, leads to the generation of OH radicals, being the chief reactive species to initiate degradation. Therefore, a basic environment supports more hydroxyl radical production and reduction in recombination between e-/h + pairs. Moreover, the electrostatic interactions between negatively charged Fe-CN-AW and positively charged RhB dye molecules increase in the basic medium. In an acidic medium or at higher pH values above 9, the repulsion

TABLE 2: ANOVA table for degradation of RhB by Fe-g-C$_3$N$_4$-Ag$_2$WO$_4$

Source	Sum of squares	Df	Mean square	F value	p value prob > F	
Model	5555.55	14	396.83	62.49	<0.0001*	
A-pH	1290.67	1	1290.67	203.25	<0.0001*	
B-catalyst dose	1232.67	1	1232.67	194.12	<0.0001*	
C-oxidant dose	192.67	1	192.67	30.34	<0.0001*	
D-time	1148.17	1	1148.17	180.81	<0.0001*	
AB	2.25	1	2.25	0.35	0.5605	
AC	36.00	1	36.00	5.67	0.0310	
AD	30.25	1	30.25	4.76	0.0454	Significant
BC	0.000	1	0.000	0.000	1.0000	
BD	156.25	1	156.25	24.61	0.0002	
CD	4.00	1	4.00	0.63	0.4398	
A^2	1211.44	1	1211.44	190.78	<0.0001*	
B^2	74.30	1	74.30	11.70	0.0038	
C^2	390.01	1	390.01	61.42	<0.0001*	
D^2	141.44	1	141.44	22.27	0.0003	
Residual	95.25	15	6.35			
Lack of fit	81.92	10	8.19	3.07	0.1136	Not significant$
Pure error	13.33	5	2.67			
Cor total	5650.80	29				
SD	2.52		R-squared		0.9831	
Mean	77.20		Adj R-squared		0.9674	
C.V.	3.26		Pred R-squared		0.9131	
Press	491.04		Adeq precision		27.897	

*Significant model terms. $Nonsignificant lack of fit is good. We want the model to fit.

between hydroxide ions and the negatively charged composite causes agglomeration and hinders the formation of hydroxyl radicals, leading to a decrease in degradation efficiency [37]. At higher catalyst dose values above optimum value, the agglomeration of Fe-CN-AW particles leads to reduced surface area for irradiation under sunlight, reducing dye removal efficiency.

Figure 9(b) shows contours and 3D plots of the interaction between oxidant dose and pH. Maximum degradation was observed at an oxidant dose of 5 mM at an optimum pH value of 8. Oxidant (H$_2$O$_2$) inhibits the recombination of e$^-$ and h$^+$ pairs. The response was observed to increase by changing the pH of the solution between values of 6 and 8. An increase in oxidant dose has led to a decline in degradation due to the recombination of hydroxyl radicals and decline in the absorption of light due to saturation. Henceforth, at an oxidant dosage of 5 mM and pH = 8, maximum degradation was observed. Figure 9(c)) shows the relationship between pH and time by a 3D contour plot. Degradation increased as the pH and time were increased until an optimum condition was achieved. This shows that pH and time are crucial factors for enhancing the overall catalytic activity. The increase in RhB degradation by Fe-CN-AW was studied until the optimum values. After that, it begins to decrease. The reason behind it was as time increased, the reaction between the catalyst and dye molecules enhanced, which enhanced the degradation. Figure 9(d) shows the relationship between catalyst dose and oxidant dose. The 3D plots show that increasing the Fe-CN-AW dose from 10 mg/100 ml improved the degradation greatly to an optimum dose of 50 mg/100 ml and an oxidant dose of 5 mM, where it showed a maximum degradation. As the

amount of catalyst is increased, the number of active sites for the dye molecules to get adsorbed also increases; eventually, degradation is increased. However, a further increase in catalyst dose resulted in slower degradation rate due to the agglomeration of particles, thus obstructing the light penetration in the solution. The presence of an oxidant prevents e$^-$/h$^+$ pairs from recombining. The improved RhB degradation is attributed to the possible reaction of Fe ions with oxidant species producing molecular oxygen species and more hydroxyl radicals leading to enhanced photocatalytic degradation [28].

From Figure 9(e), the interaction between Fe-CN-AW dosage and time is evident. It was seen that as the catalyst dose and time increased up to the optimized values, degradation also enhanced, showing a positive effect of catalyst amount and time. As the time duration of sunlight irradiation was increased from 1 hour to 2 hours and catalyst dose up to 50 mg/100 ml, the degradation increased. A further increase in dose above 50 mg at 2 hours of irradiation shows a steady decline in degradation due to the blocking of the active sites.

6. Scavenger Study and the Proposed Mechanism

To investigate the role of key scavengers for RhB degradation by ternary Fe-CN-AW under sunlight, the following conditions of experimental reaction were used: pH = 8, catalyst loading = 50 mg/100 ml, IDC = 10 ppm, H$_2$O$_2$ concentration = 5 mM, and irradiation time 120 minutes. DMSO, EDTA, K$_2$Cr$_2$O$_7$, and ascorbic acid were employed as scavenging agents for hydroxyl radicals, holes, electrons, and
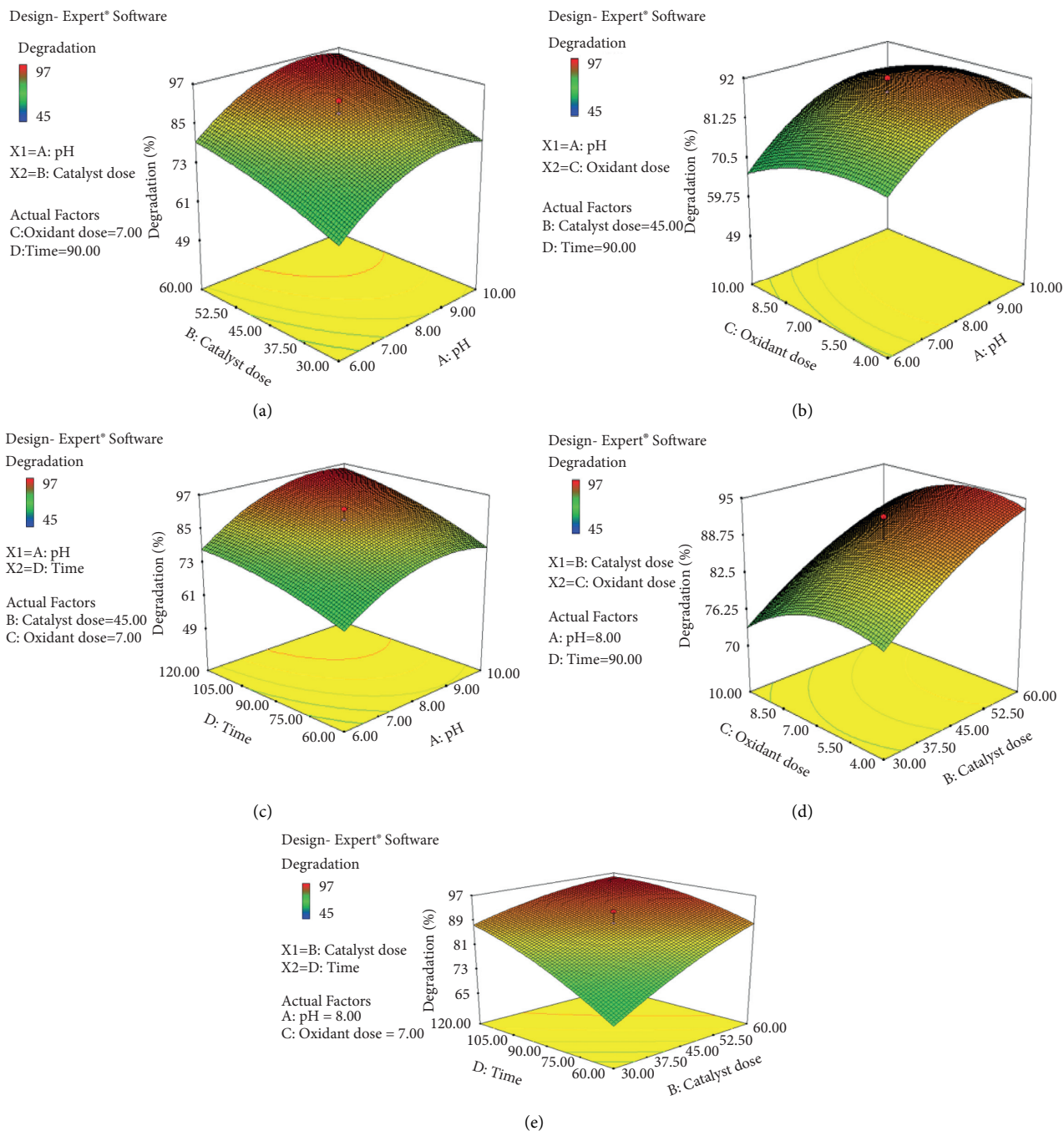
(a)

(b)

(c)

(d)

(e)

Figure 9: Response surface methodology showing the interaction of various reaction parameters. Interaction between (a) catalyst dose and pH, (b) oxidant dose and pH, (c) time and pH, (d) catalyst dose and oxidant dose, and (e) time and catalyst dosage.

superoxide radical ($O_2{}^{-2}$), respectively. The concentration of all these scavengers was kept at 5 mM during the experiments executed under sunlight. The active radical was immediately scavenged by the appropriate scavenger while the rest of the radicals carried out the dye degradation. The evaluation of the activities of the investigated scavenging agents is shown in Figure 10(a). The results indicate that the maximum reduction in catalytic activity was observed by the addition of EDTA, ascorbic acid, and then, DMSO and the least by the addition of $K_2Cr_2O_7$. Figure 10(a) shows the

decrease in degradation from 97% to 32%, 47%, 54%, and 89%, respectively. Accordingly, h^+, $\bullet O^{2-}$, and $\bullet OH$ are produced and involved in the photocatalytic reaction, while electrons play a minor role. On this basis, the proposed mechanism of Fe-CN-AW is as suggested in Figure 11.

Under visible light irradiation, both the Fe-CN and Ag_2WO_4 can be excited and produce light-induced es^- and h^+. Photoinduced es^- in the conduction band (CB) of silver tungstate is easily transferred to the Fe-CN valence band (VB). This is probably because of electrostatic interactions
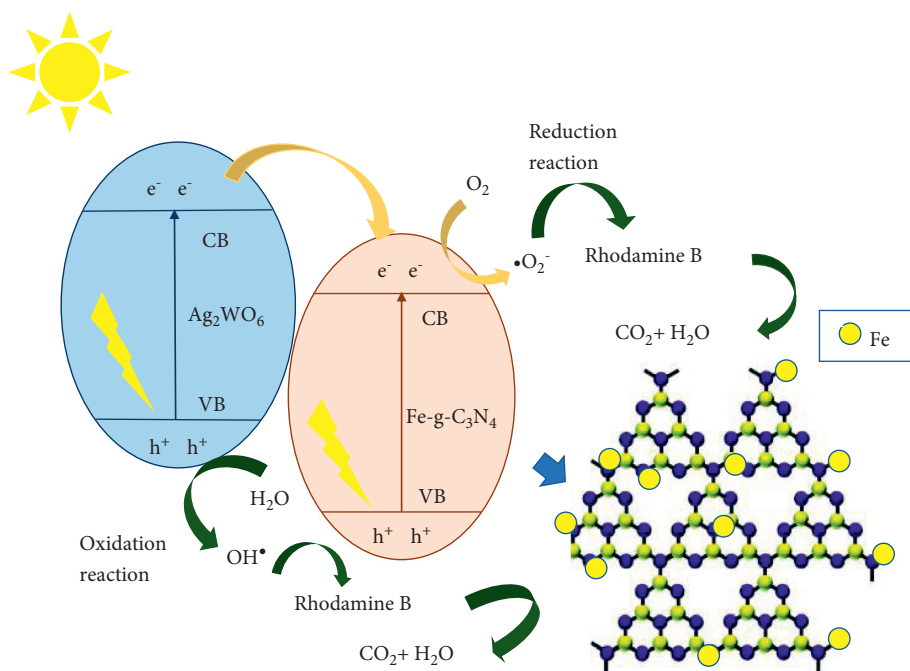
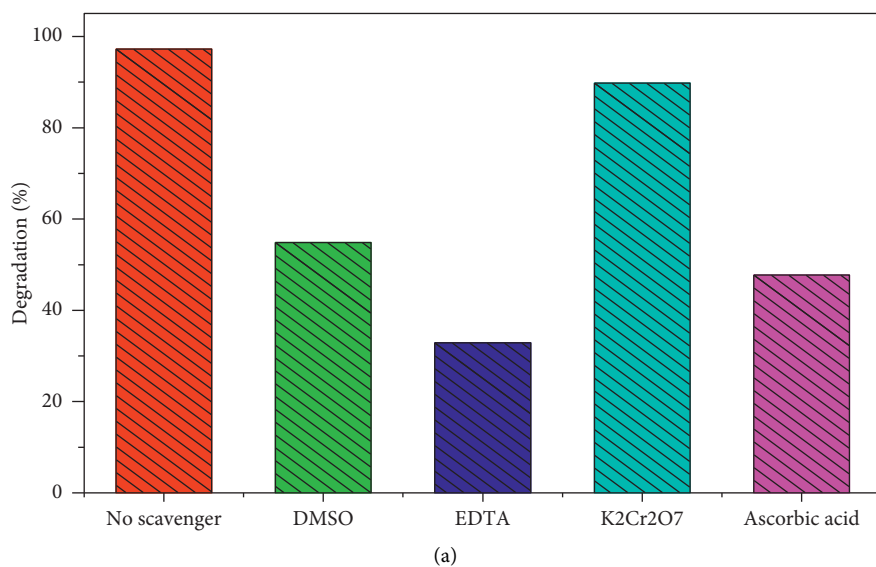FIGURE 10: Proposed mechanism of rhodamine B dye degradation using ternary Fe-CN-AW.
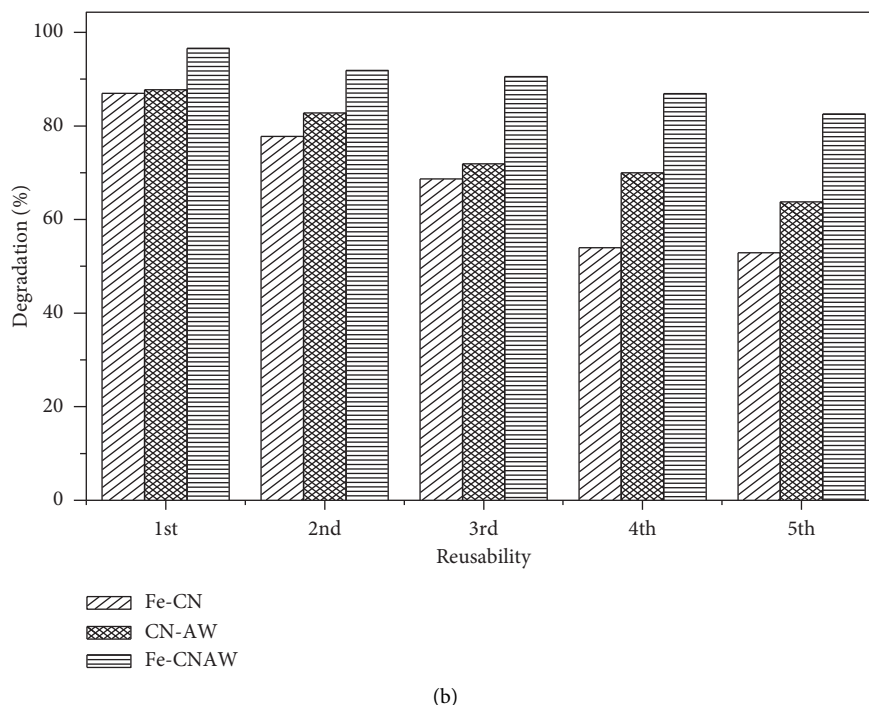

(a)

FIGURE 11: Continued.

(b)

FIGURE 11: (a) Experiment on the role of several radical scavengers and (b) reusability experiment by Fe-CN, CN-AW, and Fe-CN-AW nanocomposites.

TABLE 3: Comparison of the degradation performance of metal/nonmetal doped g-C$_3$N$_4$-based ternary photocatalysts.

Sr. no.	Photocatalysts	Fabrication methods	Target pollutants	Light source	Degradation time (min)	Photocatalytic activity (%)	References
1.	P-g–C$_3$N$_4$–ag$_2$WO$_4$	Thermal polymerization method	Indomethacin	Visible light	60	91	[11]
2.	Ag-g-C$_3$n$_4$/FeWO$_4$	Hydrothermal	Rhodamine B	Visible light	120	98	[28]
3.	P-S-g-C$_3$N$_4$/ Ag$_2$CO$_3$	Ion-exchange deposition method	2,4-Dinitrophenol	Visible light	360	99	[38]
4.	O-g-C$_3$N$_4$/ZnIn$_2$S$_4$	Hydrothermal method	2,4-Dinitrophenol	Visible light	180	92	[39]
5.	P-S-g-C$_3$N$_4$/ Ag$_2$VO$_3$	Ion-exchange deposition method	Phenol	Visible light	360	99	[40]
6.	Co/Fe-g-C$_3$N$_4$/ MOFs	Hydrothermal method	Rhodamine B	UV/Vis	30	99	[12]
7.	Fe– C$_3$N$_4$/Ag$_2$CO$_3$	Hydrothermal method	Rhodamine B	Visible light	180 minutes	97	This work

among electrons in the CB of Ag$_2$WO$_4$ and VB holes of Fe-CN, ultimately decreasing the charge carrier's recombination within the Fe-CN and Ag$_2$WO$_4$ heterojunction. The e$^-$ in the CB of Fe–CN becomes trapped by the oxygen present on the surface of the composite, forming •O^{2-}. Moreover, holes accumulated in the CB of Ag$_2$WO$_4$ react with water molecules, producing hydroxyl radicals. The generated •OH and •O^{2-} radicals then participate in the degradation process. These characteristic features of the doped ternary heterostructure lead to the enhancement of photocatalytic degradation instead of individual and binary components. The catalyst Fe-CN-AW showed 97% degradation under sunlight. A comparison of doped graphitic carbon nitride-based ternary composites is shown in Table 3.

7. Reusability

Keeping optimal conditions specified for all three catalysts, stability of all photocatalysts was confirmed by utilizing catalysts continually in 5 consecutive runs for ensuring field application. The catalysts were separated through centrifugation from the treated RhB solution, and distilled water was used for rinsing thrice. Then, samples were dried at 70°C utilizing an electric oven. All catalysts were weighed after each catalytic recycle and inspected for their efficiency of RhB removal. Reusability trials were conducted at optimized conditions for each catalyst in a time duration of two hours for all composites. No considerable catalytic activity loss was detected even after 5 experimental runs, with a minimal

reduction after the fifth run, as shown in Figure 10(b). Experimental results showed that the Fe-CN-AW ternary heterojunction has high mechanical stability and reusability.

8. Conclusions

The Fe-CN-AW is a novel ternary heterojunction that shows a remarkable result for organic dye degradation. A simple hydrothermal method was employed for the fabrication of the iron-doped ternary photocatalyst. The ternary nanocomposite exhibited exceptional rhodamine B degradation, underneath solar light irradiation. The Fe-CN-AW showed 97% RhB degradation in two hours. The improved photocatalytic efficiency was accredited to the construction of a ternary heterojunction formed because of Fe doping and coupling of graphitic carbon nitride and silver tungstate. The prominent characteristics of all components were present in the ternary heterojunction, with doping further suppressing the recombination of electrons and holes. The catalysts are very stable and show a minimal reduction in efficiency even after five repeated experiments.

Data Availability

The data used to support the findings of this study are included within the article; additional information/data will be made available upon request.

Conflicts of Interest

The authors declare no conflicts of interest.

Acknowledgments

References

[1] E. M. Pala, "Ultrastructural deformities in the scales of *Cyprinus carpio* inhabiting two government-sponsored fish farms in north-east India contaminated by municipal wastes and other pollutants," *Microscopy and Microanalysis*, vol. 24, no. 6, pp. 729–733, 2018.

[2] R. Das, "Application photocatalysis for treatment of industrial waste water-a short review," *OALib*, vol. 1, no. 5, pp. 1–17, 2014.

[3] Y. Deng and R. Zhao, "Advanced oxidation processes (AOPs) in wastewater treatment," *Current Pollution Reports*, vol. 1, no. 3, pp. 167–176, 2015.

[4] M. O. Barbosa, N. F. F. Moreira, A. R. Ribeiro, M. F. R. Pereira, and A. M. T. Silva, "Occurrence and removal of organic micropollutants: an overview of the watch list of EU Decision 2015/495," *Water Research*, vol. 94, pp. 257–279, 2016.

[5] J. Fu, "g-C3N4-based heterostructured photocatalysts," *Advanced Energy Materials*, vol. 8, no. 3, pp. 170–503, 2018.

[6] K. C. Devarayapalli, S. V. Prabhakar Vattikuti, T. V. Madhukar Sreekanth, P. Chidanandha Nagajyothi, and J. Shim, "Pyrolysis synthesized g-C 3 N 4/Nb 2 O 5 nanocomposite for enhanced photocatalytic activity under white LED light irradiation," *Chemistry*, vol. 4, no. 45, pp. 13250–13258, 2019.

[7] A. Habibi-Yangjeh and M. Mousavi, "Deposition of CuWO 4 nanoparticles over g-C 3 N 4/Fe 3 O 4 nanocomposite: novel magnetic photocatalysts with drastically enhanced performance under visible-light," *Advanced Powder Technology*, vol. 29, no. 6, pp. 1379–1392, 2018.

[8] S. V. P. Vattikuti, B. P. Reddy, C. Byon, and J. Shim, "Carbon/CuO nanosphere-anchored g-C3N4 nanosheets as ternary electrode material for supercapacitors," *Journal of Solid State Chemistry*, vol. 262, pp. 106–111, 2018.

[9] K. C. Devarayapalli, K. Lee, N. D. Nam, S. V. P. Vattikuti, and J. Shim, "Microwave synthesized nano-photosensitizer of CdS QD/MoO3-OV/g-C3N4 heterojunction catalyst for hydrogen evolution under full-spectrum light," *Ceramics International*, vol. 46, no. 18, pp. 28467–28480, 2020.

[10] S. V. P. Vattikuti, P. A. K. Reddy, J. Shim, and C. Byon, "Visible-light-driven photocatalytic activity of SnO2-ZnO quantum dots anchored on g-C3N4 nanosheets for photocatalytic pollutant degradation and H2 production," *ACS Omega*, vol. 3, no. 7, pp. 7587–7602, 2018.

[11] J. Huang, "Ultrathin Ag2WO4-coated P-doped g-C3N4 nanosheets with remarkable photocatalytic performance for indomethacin degradation," *Journal of Hazardous Materials*, vol. 392, p. 122355, 2020.

[12] P. Liu, "Co/Fe co-doped porous graphite carbon derived from metal organic framework for microelectrolysis-Fenton catalytic degradation of Rhodamine B," *Journal of Environmental Chemical Engineering*, vol. 9, no. 5, Article ID 105924, 2021.

[13] S. Kumar, "Visible light-assisted photodegradation by silver tungstate-modified magnetite nanocomposite material for enhanced mineralization of organic water contaminants," *Applied Nanoscience*, vol. 10, pp. 1–15, 2019.

[14] J. Chen, "Fabrication of hierarchical sheet-on-sheet WO3/g-C3N4 composites with enhanced photocatalytic activity," *Journal of Alloys and Compounds*, vol. 777, pp. 325–334, 2019.

[15] P. Praus, "Graphitic carbon nitride: synthesis, characterization and photocatalytic decomposition of nitrous oxide," *Materials Chemistry and Physics*, vol. 193, pp. 438–446, 2017.

[16] K. Dai, "A facile fabrication of plasmonic g-C3N4/Ag2WO4/Ag ternary heterojunction visible-light photocatalyst," *Materials Chemistry and Physics*, vol. 177, pp. 529–537, 2016.

[17] S. Tonda, "Fe-doped and-mediated graphitic carbon nitride nanosheets for enhanced photocatalytic performance under natural sunlight," *Journal of Materials Chemistry*, vol. 2, no. 19, pp. 6772–6780, 2014.

[18] T. Li, "Mechanisms for highly efficient mineralization of bisphenol A by heterostructured Ag2WO4/Ag3PO4 under simulated solar light," *ACS Sustainable Chemistry & Engineering*, vol. 7, no. 4, pp. 4177–4185, 2019.

[19] P. Raizada, A. A. P. Khan, and P. Singh, "Construction of carbon nanotube mediated Fe doped graphitic carbon nitride and Ag3VO4 based Z-scheme heterojunction for H2O2 assisted 2, 4 dimethyl phenol photodegradation," *Separation and Purification Technology*, vol. 247, p. 116957, 2020.

[20] B. Zhu, "Fabrication and photocatalytic activity enhanced mechanism of direct Z-scheme g-C3N4/Ag2WO4 photocatalyst," *Applied Surface Science*, vol. 391, pp. 175–183, 2017.

[21] S. Honary, "Green synthesis of silver nanoparticles induced by the fungus Penicillium citrinum," *Tropical Journal of Pharmaceutical Research*, vol. 12, no. 1, pp. 7–11, 2013.

[22] K. Devarayapalli, "Mesostructured g-C3N4 nanosheets interconnected with V2O5 nanobelts as electrode for

coin-cell-type-asymmetric supercapacitor device," *Materials Today Energy*, vol. 21, p. 100699, 2021.

[23] M. U. Rahman, "Solar driven photocatalytic degradation potential of novel graphitic carbon nitride based nano zero-valent iron doped bismuth ferrite ternary composite," *Optical Materials*, vol. 120, p. 111408, 2021.

[24] X. Wang, "Recyclable nanoscale zero valent iron doped g-C3N4/MoS2 for efficient photocatalysis of RhB and Cr (VI) driven by visible light," *ACS Sustainable Chemistry & Engineering*, vol. 4, no. 7, pp. 4055–4063, 2016.

[25] N. Nadeem, "Degradation of reactive dye using heterogeneous photo-Fenton catalysts: ZnFe2O4 and GO-ZnFe2O4 composite," *Materials Research Express*, vol. 7, no. 1, p. 015519, 2020.

[26] N. Tahir, "Fabrication of visible light active Mn-doped Bi2WO6-GO/MoS2 heterostructure for enhanced photocatalytic degradation of methylene blue," *Environmental Science and Pollution Research*, pp. 1–16, 2021.

[27] C. V. Reddy, "Mn-doped ZrO2 nanoparticles prepared by a template-free method for electrochemical energy storage and abatement of dye degradation," *Ceramics International*, vol. 45, no. 12, pp. 15298–15306, 2019.

[28] R. Saher, "Sunlight-driven photocatalytic degradation of rhodamine B dye by Ag/FeW 4/gC3N4 composites," *International journal of Environmental Science and Technology*, vol. 18, no. 4, pp. 927–938, 2021.

[29] J. F. Moulder, *Handbook of X-Ray Photoelectron Spectroscopy*, pp. 230–232, Perkin-Elmer Corporation, Waltham, MA, UA, 1995.

[30] B. Yu, "Functionalized graphene oxide/phosphoramide oligomer hybrids flame retardant prepared via in situ polymerization for improving the fire safety of polypropylene," *RSC Advances*, vol. 4, no. 60, pp. 31782–31794, 2014.

[31] P. Li, "Carboxyl groups on g-C3N4 for boosting the photocatalytic U (VI) reduction in the presence of carbonates," *Chemical Engineering Journal*, vol. 414, pp. 12–88, 2021.

[32] R. Ahmad, "Photocatalytic systems as an advanced environmental remediation: recent developments, limitations and new avenues for applications," *Journal of Environmental Chemical Engineering*, vol. 4, no. 4, pp. 4143–4164, 2016.

[33] A. Rafiq, "Photocatalytic degradation of dyes using semiconductor photocatalysts to clean industrial water pollution," *Journal of Industrial and Engineering Chemistry*, vol. 97, 2021.

[34] M. Abdellah, "Photocatalytic decolorization of methylene blue using TiO2/UV system enhanced by air sparging," *Alexandria engineering journal*, vol. 57, no. 4, pp. 3727–3735, 2018.

[35] N. Nadeem, "Improved photocatalytic degradation of dye using coal fly ash-based zinc ferrite (CFA/ZnFe2O4) composite," *International journal of Environmental Science and Technology*, pp. 1–16, 2021.

[36] I. D. Tunç, "Growth of ZnO nanowires on carbon fibers for photocatalytic degradation of methylene blue aqueous solutions: an investigation on the optimization of processing parameters through response surface methodology/central composite design," *Ceramics International*, vol. 46, no. 6, pp. 7459–7474, 2020.

[37] S. Mortazavian, A. Saber, and D. E. James, "Optimization of photocatalytic degradation of Acid Blue 113 and Acid Red 88 textile dyes in a UV-C/TiO2 suspension system: application of response surface methodology (RSM)," *Catalysts*, vol. 9, no. 4, pp. 300–360, 2019.

[38] P. Raizada, "Visible light assisted photodegradation of 2, 4-dinitrophenol using Ag2CO3 loaded phosphorus and sulphur co-doped graphitic carbon nitride nanosheets in simulated wastewater," *Arabian Journal of Chemistry*, vol. 13, no. 1, pp. 3196–3209, 2020.

[39] A. Uddin, "Hydrothermal synthesis of 3D/2D heterojunctions of ZnIn2S4/oxygen doped g-C3N4 nanosheet for visible light driven photocatalysis of 2, 4-dichlorophenoxyacetic acid degradation," *Journal of Alloys and Compounds*, vol. 845, p. 156206, 2020.

[40] P. Raizada, "Fabrication of Ag3VO4 decorated phosphorus and sulphur co-doped graphitic carbon nitride as a high-dispersed photocatalyst for phenol mineralization and *E. coli* disinfection," *Separation and Purification Technology*, vol. 212, pp. 887–900, 2019.